JACS
JOURNAL OF THE AMERICAN CHEMICAL SOCIETY
pubs.acs.org/JACS
Article

Simultaneous Two-Color Visualization of Lipid Droplets and Endoplasmic Reticulum and Their Interplay by Single Fluorescent Probes in Lambda Mode

Lifang Guo, Minggang Tian, Zhiyun Zhang, Qing Lu, Zhiqiang Liu, Guangle Niu,* and Xiaoqiang Yu*

Cite This: J. Am. Chem. Soc. 2021, 143, 3169−3179
Read Online

ABSTRACT: In living systems, subcellular organelles mutually cooperate and closely contact to form organelle interaction networks. Thus, the simultaneous and discriminative visualization of different organelles is extremely valuable for elucidating their distribution and interplay. However, such meaningful investigations remain a great challenge due to the lack of advanced single fluorescent probes (SF-probes) capable of simultaneous and two-color imaging of two targets. Herein, for the first time, we present two excited-state intramolecular proton transfer (ESIPT) based SF-probes (PPC and EPC) for simultaneous two-color fluorescence imaging of lipid droplets (LDs) and the endoplasmic reticulum (ER) under single-wavelength excitation. Due to the strong electron-donating ability of the side substituents, the fluorescence spectra and colors of these ESIPT probes are highly sensitive to the nuance of water contents between LDs and ER, leading to orange and green fluorescence in LDs and ER, respectively, in the Lambda imaging mode. Using the probe PPC or EPC, the morphology, size, and distribution of LDs and ER have been investigated in live cells and tissues. With the aid of *in situ* and real-time fluorescence imaging in Lambda mode, we observed the generation of newborn LDs near the ER regions and their close apposition and shared identical fluorescence colors, probably providing a valuable proof for the mainstream hypothesis that LDs originate from the ER. The remarkable imaging performances render these SF-probes as powerful tools to decipher LD-ER related biological processes.

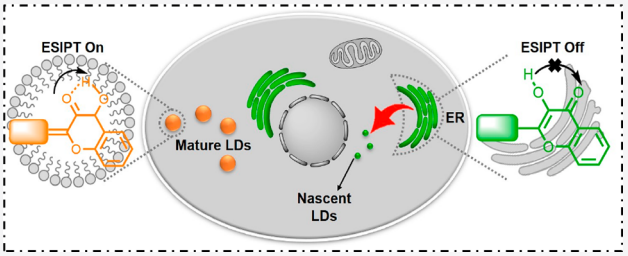

INTRODUCTION

As the basic unit in cells, subcellular organelles play indispensable and significant roles in diverse biological processes.[1−3] Generally, these spatially distributed organelles show unique functionalities. Besides, they also mutually cooperate and closely contact to form organelle interaction networks for completing complex biological events.[4,5] Thus, it is extremely valuable to investigate the distributions and interactions of those closely related organelles. Lipid droplets (LDs), as highly dynamic organelles, not only play vital roles in lipid metabolism and homeostasis but also display multiple functional interactions with other organelles, especially the endoplasmic reticulum (ER).[6−9] Currently, it is believed by a mainstream hypothesis that LDs are derived from the ER.[6,7] There are two reasons for this: first, electron micrographs reveal that LDs are close to the ER in space; second, LD proteome studies show that enzymes used to catalyze the synthesis of LDs neutral lipids are principally located in the ER.[8,9] However, these indirect observations are based on fixed or dead samples, which may result in distorted and incorrect information. Therefore, the development of an effective method to directly visualize and study LDs and the ER as well as their interplay in live samples is a particularly significant yet challenging task.

Fluorescent probes have become powerful tools for versatile biomedical imaging in live cells, due to their unique advantages of excellent spatial resolution, remarkable sensitivity, high selectivity, noninvasiveness, and *in situ* property.[10−17] Recently, some impressive works have been achieved for LD[18−25] or ER[26−29] imaging by multiple fluorescent probes. However, to the best of our knowledge, only a few probes have been developed for simultaneous LD and ER imaging with one emission color,[30,31] inevitably leading to many difficulties in the simultaneous and discriminative visualization and analysis of LDs and the ER and their interaction. To address this concern, one possible way is the combined use of two different organelle-targeted probes. However, some existing drawbacks probably restrict the further practical application of this strategy: the tedious staining and washing procedure, unsatisfying spectral cross-talk, and increased cytotoxicity to live samples.[32] Therefore, it is desirable to develop single fluorescent probes (SF-

Received: November 25, 2020
Published: February 11, 2021

https://dx.doi.org/10.1021/jacs.0c12323
J. Am. Chem. Soc. 2021, 143, 3169−3179

probes) for simultaneous and two-color imaging of LDs and ER and their associated interaction. However, such a fluorescent probe has not yet been reported.

Generally, the fluorescence imaging system contains two multicolor imaging modes: the multichannel mode and the Lambda mode.[33] Multichannel mode based fluorescence imaging is widely used by confocal laser scanning microscopy in live samples.[34] However, this imaging method fails to give the real emission color but only displays the pseudocolor of dyes or probes, probably resulting in spectral cross-talk and inaccurate staining information.[33] In comparison with the multichannel mode, fluorescence imaging in the Lambda mode exhibits a much more powerful character, which can obtain the real-color emission in one scan imaging, avoid spectral cross-talk in subchannel imaging, and give more clear and definite labeling information.[35] In addition, Lambda mode based fluorescence imaging can discriminate one stained region from another with distinct emission colors, which is particularly useful for simultaneously imaging different organelles with similar and close emission spectra.

LDs consist of a neutral core and a phospholipid monomembrane.[6] For efficient storage of triglycerides and cholesterol esters in the neutral core, water is barely not included.[36] However, the ER is a bilayer membrane structure containing some lipophilic components and a certain water content. On the basis of the different water contents between LDs and the ER, we anticipated that a lipophilic water-sensitive fluorescent probe should be able to achieve simultaneous staining of LDs and the ER as well as selective discrimination by two different fluorescence colors. Toward this end, excited-state intramolecular proton transfer (ESIPT) based probes are promising design choices, because ESIPT molecules can show two well-separated emissions of normal (N*) and tautomeric (T*) states and the fluorescence intensity ratio of N*/T* generally changes with the surrounding environments.[37−39] Especially, the ESIPT process involves the formation of intramolecular hydrogen bonds in the excited state;[40−42] thus, ESIPT-based probes are prone to be inhabited by protic solvents (such as water) via the formation of intermolecular hydrogen bonds. As a result, the fluorescence intensity ratio N*/T* depends strongly on the protic solvent contents, probably resulting in the distinct fluorescence colors.

Herein, on the basis of the classical ESIPT skeleton 3-hydroxyflavone,[43−45] we designed and synthesized three fluorescent probes (PPC, EPC, and MNC) by introducing different side substituent groups (Scheme 1). On the one hand, different side substituents can tune the lipophilicity of probes to improve the ability of targeting LDs and the ER, with the premise of retaining ESIPT properties. On the other hand, the different electron-donating groups probably influence the fluorescence response sensitivity of these probes to different water-containing environments. The experimental results showed that these probes could target both LDs and the ER, due to the appropriate lipophilicity respectively with Clog *P* values of 6.65, 4.28, and 4.13.[46] Among them, PPC and EPC displayed high sensitivity to slight variations in water content, thus enabling two-color imaging of LDs and the ER in Lambda mode. However, the water-insensitive probe MNC could not discriminate LDs and the ER by color. For a clear explanation of the above phenomena and a better understanding of the structure/ESIPT properties, experimental and theoretical studies by a further comparison with the newly synthesized control probe PC without an electron donor substituent were carried out. The results demonstrated that ESIPT dyes with side substituents of strong electron-donating ability showed high sensitivity to slight water content changes, because their ESIPT processes were prone to be influenced by the water-containing microenvironment. In addition, using the probe PPC or EPC, the distribution relationships between LDs and the ER in live cells and tissues have been visualized and mapped. Further, the relationship between LD biogenesis and the ER was also investigated, which probably provides a very helpful proof for the mainstream hypothesis that LDs are generated from the ER.

Scheme 1. Schematic Illustration of Two-Color Visualization of Lipid Droplets (LDs) and ER Using ESIPT-Active Fluorescent Probes PPC and EPC and the Control Probe MNC

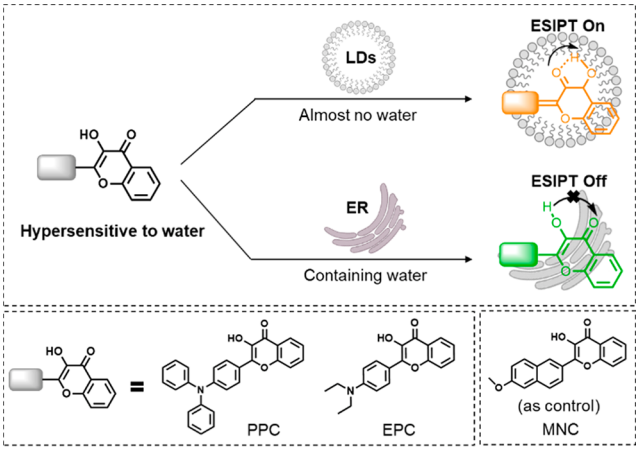

RESULTS AND DISCUSSION

Synthesis. The synthesis routes of the 3-hydroxyflavone-based fluorescent probes PPC, EPC, and MNC are depicted in Scheme S1. First, commercially available aromatic aldehydes (compounds **1a−c**) were reacted with compound **2** in the presence of NaOH in EtOH solution, leading to the crucial intermediate compounds **3a−c** via a simple nucleophilic reaction. Then the final probes PPC, EPC, and MNC were obtained by cyclization and oxidation reactions of compound **3** under further treatment of NaOH and H_2O_2. The probes PPC, EPC, and MNC were well characterized by ^{1}H NMR, ^{13}C NMR, and HRMS. The detailed synthesis and characterization data (Figures S1−S9) are shown in the Supporting Information.

Photophysical Properties. Before performing photophysical experiments, we first optimized the structures of these probes using the Gaussian 09 program package.[47] As shown in Figure 1, the distances between H and O of the three probes were about ∼2.0 Å, suitable for forming the intramolecular hydrogen bonding and structural rearrangement in the excited state, indicating the occurrence of an ESIPT process.[39] Further, we investigated their absorption and emission spectra in a variety of solvents (Figure 1 and Figure S13 and Table S1). PPC exhibited almost the same absorption peak at 400 nm in various solvents, yet it had different emission behaviors. In aprotic solvents such as 1,4-dioxane, it showed two emission bands with nearly 100 nm separation, including a short-wavelength emission at 483 nm from N* state and a long-wavelength emission peaking at 582 nm from T* state, which indicated the existence of ESIPT. In protic or highly polar solvents, the ESIPT process was inhabited and PPC only showed the N* state emission with a maximum band at about 540 nm, in which the

https://dx.doi.org/10.1021/jacs.0c12323
J. Am. Chem. Soc. 2021, 143, 3169−3179

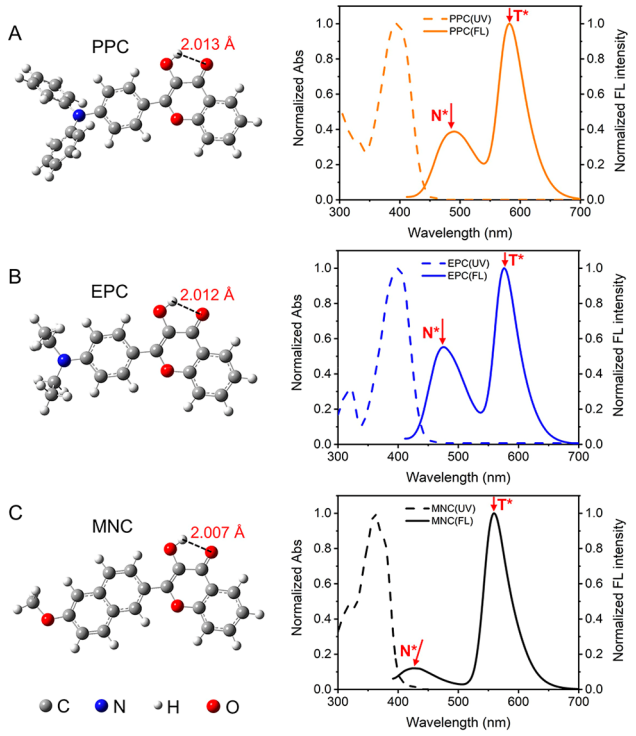

Figure 1. Optimized structures and normalized absorption (dashed lines) and fluorescence emission (solid lines) spectra of (A) PPC, (B) EPC, and (C) MNC in 1,4-dioxane. For PPC and EPC, λ_{ex} = 405 nm; for MNC, λ_{ex} = 385 nm.

red-shifted band of the N* state in comparison with that in 1,4-dioxane may be due to the formation of a hydrogen bond between PPC and ambient solvents. Likewise, EPC displayed results similar to those of PPC. However, MNC exhibited blue-shifted absorptions and emissions due to its weak electron-donating ability, with a maximum absorption band at 365 nm and maximum emission bands at about 450 and 559 nm. Additionally, the three probes showed moderate molar extinction coefficients and fluorescence quantum yields in various solvents, suitable for bioimaging. These data are also summarized in Table S1.

Fluorescence Sensitivity toward Water-Containing Microenvironments. We then investigated the emission behaviors of PPC, EPC, and MNC to different water contents. Herein, mixtures of 1,4-dioxane (aprotic solvent) and water with different water fractions were used as the testing environments. As shown in Figure 2 and Table S2, PPC showed a superimposed strong orange fluorescence of 582 nm at the T* state and 483 nm at the N* state in 1,4-dioxane. With an increased water fraction (f_w) from 0% to 10%, the fluorescence intensity of the N* state was remarkably enhanced while the T* state emission showed a slight decrease. According to the Commission International de L'Eclairage (CIE) chromaticity coordinates[48] in Figure 2A and Table S3, the corresponding fluorescence colors showed distinct variations from orange to green, accompanied by the coordinates changing from (0.44, 0.41) to (0.34, 0.56). When f_w was over 10%, the T* state emission disappeared and only the N* state emission was left with green fluorescence (Figure S14A). The above results demonstrated that PPC is highly sensitive to slight water-content changes. In addition, EPC also exhibited phenomena similar to those of PPC (Figure 2B and Figure S14B and Tables S2 and S3). However, MNC was inert to the water fractions in the range of 0−10% in comparison with PPC and EPC, showing orange fluorescence with almost no changes (Figure 2C and Tables S2 and S3). It is worth noting that MNC began to show visible variations when the water content was increased to 20% (Figure S14C), indicating that MNC could respond to water-rich media but is not sensitive to a slight amount of water. In addition, the three probes also showed results in mixtures of 1,4-

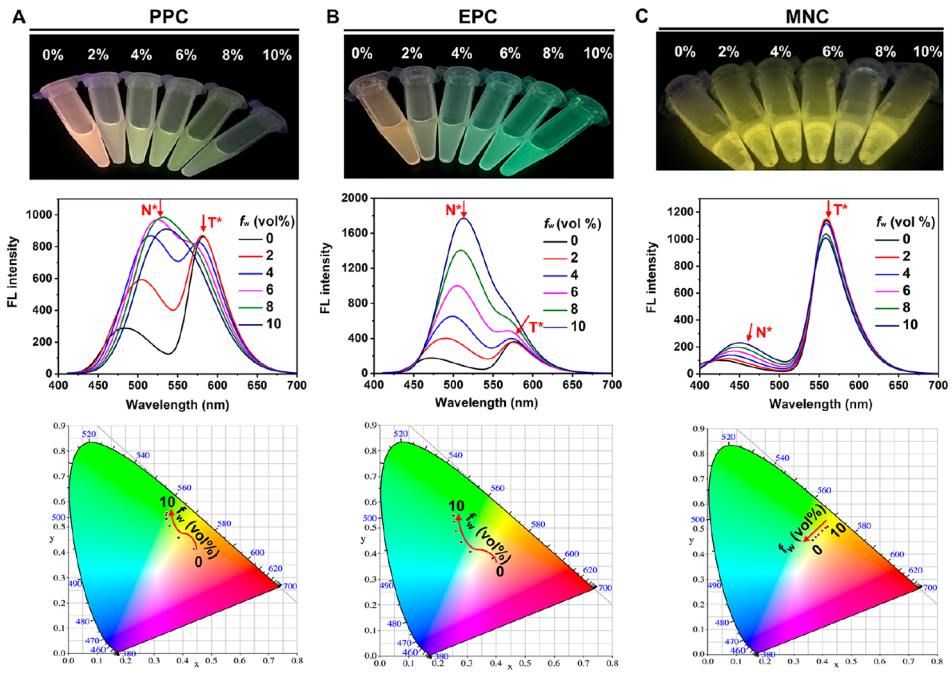

Figure 2. Fluorescence photos under 365 nm excitation of a hand-held ultraviolet lamp, fluorescence spectra, and CIE1931 coordinates of (A) PPC, (B) EPC, and (C) MNC in 1,4-dioxane/water mixtures with different water fractions (f_w). For PPC and EPC, λ_{ex} = 405 nm; for MNC, λ_{ex} = 385 nm.

https://dx.doi.org/10.1021/jacs.0c12323
J. Am. Chem. Soc. 2021, 143, 3169−3179

dioxane and MeOH similar to those in 1,4-dioxane and water mixtures (Figures S15 and S16 and Table S4).

Discussion of Structure/ESIPT Properties. The 3-hydroxyflavone-based ESIPT probes PPC, EPC, and MNC showed variable fluorescence responses to water, which can probably be attributed to their different side substituent groups. Given the different electron-donating abilities of a diphenylamino group, a diethylamino group, and a methoxyl group, we speculated that the strong electron-donating ability of side substituent groups could contribute to the ESIPT property with highly sensitive fluorescence responses to water. To prove this conjecture, we synthesized the control ESIPT dye 3-hydroxyflavone (denoted PC, Figure S17A) without an electron-donating group substituent in comparison with PPC and EPC. Its synthesis route is depicted in Scheme S1, and the ^{1}H NMR, ^{13}C NMR, and HR-MS spectra are shown in Figures S10−S12 in the Supporting Information. As expected, PC showed two different emission peaks conforming to the ESIPT characteristics (Figure S17B,C). Then we tested the fluorescence changes of PC to different water fractions (f_w). As shown in Figure 3A, with an increase in the f_w value from 0% to 10%, PC

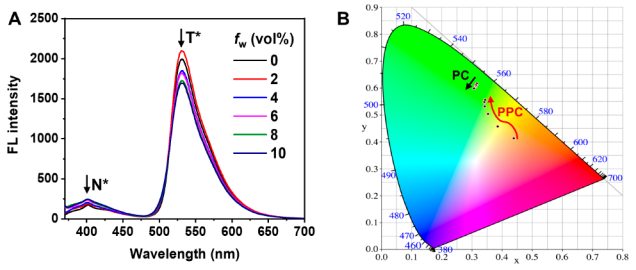

C

Property	EPC	PPC	MNC	PC
The ^{1}H NMR chemical shift of hydroxyl hydrogen	9.467	9.147	9.681	9.644
The distance between hydroxy H and ketonic O	2.013	2.012	2.007	2.010

Figure 3. (A) Fluorescence spectra and (B) CIE1931 coordinates of PC in 1,4-dioxane/water mixtures with different water fractions (f_w). The CIE1931 coordinates of PPC were also plotted as a contrast. (C) ^{1}H NMR chemical shifts (in units of ppm) of the hydroxyl hydrogen and the distances (in units of Å) between the hydroxyl H and ketonic O of PPC, EPC, MNC, and PC. λ_{ex}(PC) = 360 nm.

just showed a slight decrease in the emission intensity. It only could exhibit obvious fluorescence responses with an f_w value of above 20% (Figure S18). Obviously, its emission behaviors were very similar to those of MNC due to the weak electron-donating group substituent (Figure 2C and Figure S16C). In sharp contrast, the strong electron-donating group substituted PPC or EPC exhibited highly sensitive fluorescence responses to slight water changes from f_w = 0 to 10% (Figure 2A,B). Additionally, the fluorescence color changes in different water-content environments were revealed in CIE1931 coordinates (Figures 2 and 3B and Figure S15 and Table S5). The notable emission color changes of PPC or EPC from orange to green can be clearly seen, while those of MNC or PC almost remained unchanged. The above photophysical results confirm that our ESIPT probes with a strong electron-donating substituent group are prone to show highly sensitive fluorescence changes to the water microenvironment.

To gain a better understanding of the different ESIPT properties of these 3-hydroxyflavone-based fluorescent probes, we further investigated the intrinsic reasons by ^{1}H NMR spectra and density functional theory (DFT) calculations. As shown in their ^{1}H NMR spectra (Figure S19), the chemical shift of the hydroxyl hydrogen of MNC and PC was obviously in the lower-field region in comparison with PPC and EPC. The corresponding chemical shift values are summarized in Figure 3C. The ^{1}H NMR data indicated that the hydroxyl hydrogens of MNC and PC easily ionize to form an intramolecular hydrogen bond with the ketonic oxygen and further lead to the ESIPT process under photoexcitation. This is quite consistent with the experimental results in Figures 2 and 3A: the T* state emission of MNC and PC was dominant in comparison with PPC and EPC in the same solvent (such as 1,4-dioxane), indicating that MNC and PC were apt to undergo an ESIPT process. In addition, the optimized structure of PC was obtained (Figure S20), and the corresponding O−H distance values of PPC, EPC, MNC, and PC are summarized in Figure 3C. We could see that the O−H distances of MNC and PC were shorter than those of PPC and EPC. The results revealed that the intramolecular hydrogen bond formed in MNC and PC is more stable than those of PPC and EPC, demonstrating that their ESIPT processes can hardly be influenced a protic solvent (such as water) containing microenvironment. Therefore, the ^{1}H NMR spectra together with the theoretical analysis demonstrated that our ESIPT probes PPC and EPC with strong electron-donating substituent groups are prone to undergo the ESIPT process due to their relatively weak intramolecular hydrogen bonding and thus their fluorescence is highly sensitive to low-water-content environment changes.

Simultaneous Two-Color Imaging of LDs and the ER in Live Cells. On consideration of the similar lipidlike but different water-containing environments of LDs and the ER, the lipophilic ESIPT-active probes PPC and EPC with high fluorescence sensitivity toward slight water changes are expected to distinguish these subcellular structures with two distinct colors in the Lambda mode. Herein, PPC, EPC, and MNC were used to stain live HeLa cells. From confocal laser scanning microscopy, bright fluorescent dots could be clearly observed in the cytoplasm (Figure S21). In addition, the corresponding enlarged images showed that these fluorescent particles were well overlapped with the globular organelles with a highly refractive index in differential interference contrast (DIC), which were considered to be LDs. In addition, they also labeled the reticulate regions almost distributed in the whole cells, which may be the ER as judged by experience. The above results implied that these probes can both stain LDs and another subcellular structure. Encouraged by these results, we then studied their real-color imaging and corresponding *in situ* fluorescence spectra by using the Lambda mode (Figure 4). We could clearly see that PPC or EPC showed bright orange emission in globular LDs and green emission in the ER-like region. According to the *in situ* fluorescence spectra, the orange light in very low water-containing LDs was mainly contributed by the long-wavelength emission of the T* state. However, the green color in high water-containing subcellular regions should be the superimposed fluorescence from N* and T* states. In sharp contrast, MNC only displayed yellow fluorescence with an *in situ* emission band of about 570 nm in the whole cytoplasm, and we could not visually identify LDs from the emission color. These interesting two-color imaging results are in good accordance with the photophysical data in solution (Figure 2). The water-hypersensitive probes PPC and EPC can clearly

https://dx.doi.org/10.1021/jacs.0c12323
J. Am. Chem. Soc. 2021, 143, 3169−3179

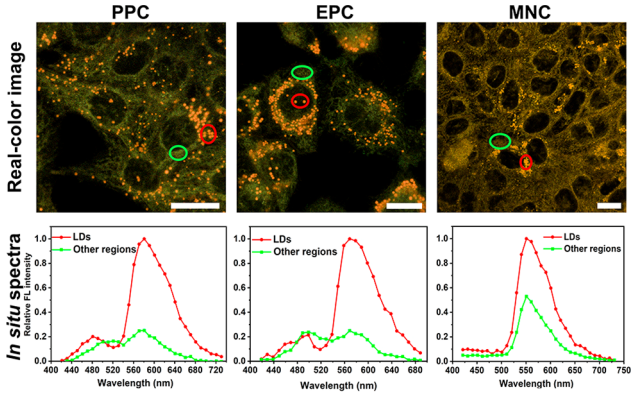

Figure 4. Real-color fluorescent images and *in situ* fluorescence spectra of LDs (indicated by the red circles) and the ER (indicated by the green circles) in live HeLa cells stained with PPC, EPC, and MNC for 2 min. λ_{ex} = 405 nm. Scale bar: 20 μm.

differentiate LDs from the ER-like regions in two different colors by using the powerful Lambda mode.

According to the *in situ* fluorescence spectra in Figure 4 and multichannel fluorescence imaging results in Figure 5A, both LDs and ER-like regions are visible in the emission range of 450−550 nm. LDs could be selectively visualized with emission collected from 600 to 700 nm, while the fluorescence of the ER could hardly be seen in this region. Thus, we could evaluate the staining location of our probes PPC and EPC by using the colocalization coefficients in some regions of interest (ROIs) indicated by the white circles in Figure 5B,C. Herein, the commercially available LD probe (BODIPY 493/503) or ER probe (ER-Tracker Red) were used to costain with PPC or EPC. As shown in Figure 5B, the fluorescence of PPC showed an excellent overlap (colocalization coefficient of 0.94) with that of BODIPY 493/503, fully indicating that the sphere dots stained by PPC were indeed LDs. For other subcellular regions stained by PPC, it was also clearly demonstrated to be the ER, due to the high colocalization coefficient of 0.87 with ER-Tracker Red (Figure 5C). Likewise, EPC could also be confirmed to be located in LDs and the ER by the satisfying colocalization data with BODIPY 493/503 and ER-Tracker Red, respectively (Figure S22). It should be noted that there is no spectral cross-talk between our probes and the two commercially available probes (Figure S23). When these results are taken together, PPC and EPC can be utilized for simultaneous visualization of LDs and the ER in a two-color imaging mode.

Cytotoxicity, Photostability, and Two-Color Imaging in Other Live Samples. As a key parameter of fluorescent probes in biological applications, the cytotoxicity of PPC and EPC was assessed with the standard MTT assay before further bioimaging. As depicted in Figure S24, the cell viability after culturing with 1 μM PPC or EPC for 2, 12, and 24 h was above 90%, and the cells treated with different concentrations (1, 4, and 10 μM) of PPC or EPC for 24 h also showed more than 90% viability. Thus, MTT data indicated that PPC and EPC possessed high biocompatibility and negligible cytotoxicity to live cells in the micromolar concentration range.

The photostability of the probes PPC and EPC was further evaluated. As shown in Figure S25, under a continuous 405 nm laser irradiation for 12 min in the Lambda mode, the fluorescent images of HeLa cells stained with PPC or EPC showed almost no fluorescence loss (Figure S25A), and the corresponding fluorescence intensity still kept 88% and 93% of the initial fluorescence intensity, respectively (Figure S25B). Therefore, the ESIPT probes PPC and EPC are very photostable and can be

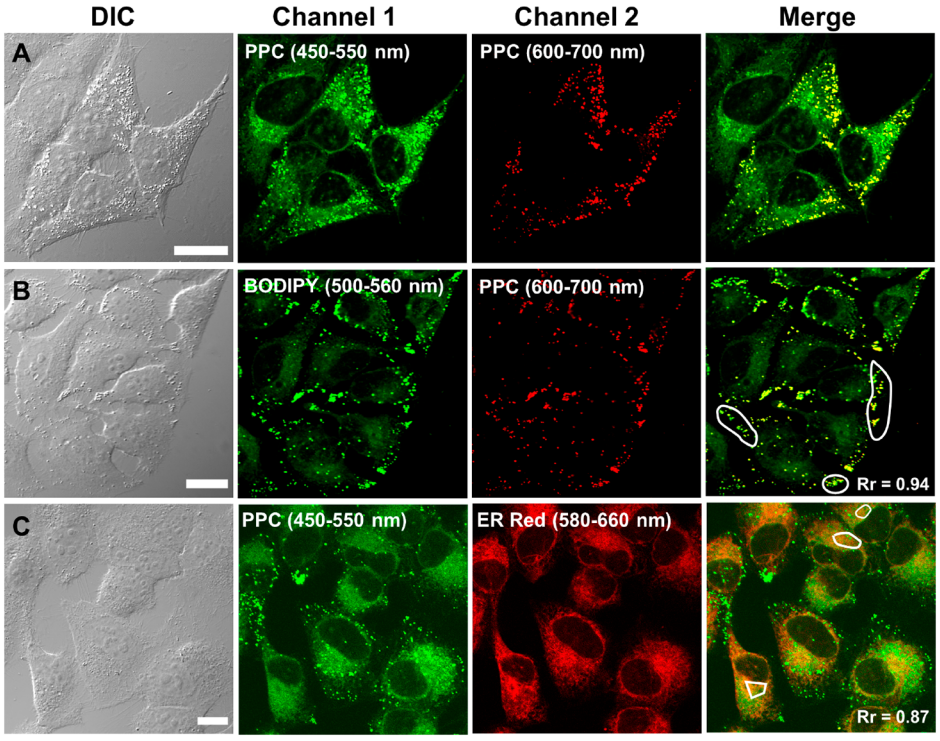

Figure 5. (A) Confocal fluorescent images of HeLa cells stained with PPC. Colocalization experiments of HeLa cells stained with PPC and (B) BODIPY 493/503 or (C) ER Red. Rr is the average colocalization coefficient of these ROIs indicated by the white circles. λ_{ex}(PPC) = 405 nm; λ_{ex}(BODIPY) = 473 nm; λ_{ex}(ER Red) = 543 nm. Scale bar: 20 μm.

https://dx.doi.org/10.1021/jacs.0c12323
J. Am. Chem. Soc. 2021, 143, 3169−3179

used to study LD- and ER-related dynamic changes in Lambda mode based fluorescence imaging.

In order to exclude the influence of cell heterogeneity on staining behaviors, the real-color fluorescence images and corresponding *in situ* fluorescence spectra were also obtained in SiHa cells and mesenchymal stem cells (MSCs) by using the Lambda mode (Figure 6 andFigure S26). It can be easily seen

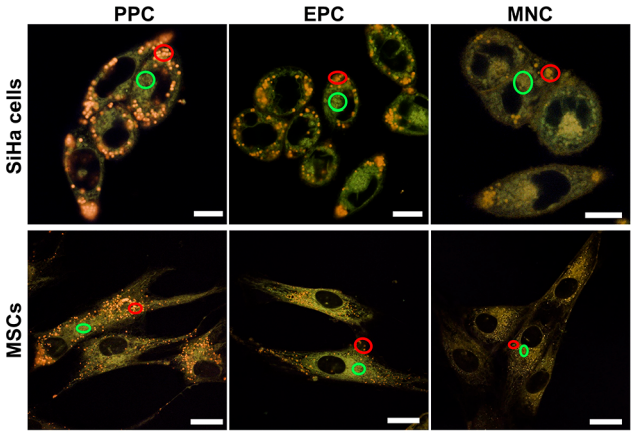

Figure 6. Real-color fluorescent images of live SiHa and MSCs stained with PPC, EPC, and MNC. The ROIs indicated by the red and green circles are analyzed for the *in situ* fluorescence spectra of LDs and the ER, respectively. λ_{ex} = 405 nm. Scale bar:10 μm (SiHa cells) or 20 μm (MSCs).

that both PPC and EPC emitted two different fluorescence colors in LDs and the ER in these cell lines, while the probe MNC still stained LDs and the ER in only one color. The above results confirmed that the staining behaviors of PPC and EPC are not affected by the cell lines in our study, and they can be used as universal tools for two-color imaging of LDs and ER.

In comparison with isolated culture cells, tissues provide the real environment for cell survival and thus can give more accurate and reliable information.[49] In different types of tissues, the morphology, distribution, and size of LDs and the ER may be diverse, due to their elaborate functions in specific tissues. Thus, simultaneous visualization of LDs and the ER with different colors in various tissues by a SF-probe is also very imperative. Herein, to indicate the accurate cell locations, the commercial far-red nucleic acid probe SYTO 61 was used for costaining with PPC or EPC. As shown in Figures S27 and S28, the real-color images of PPC or EPC in the Lambda mode was merged with the pseudocolor images of SYTO 61 in different live tissues, including heart, liver, spleen, and skeletal muscle tissues. In these tissues, LDs were tightly close to the the ER. Especially, as the main storage places of LDs,[50] heart and liver tissues had obviously more and larger-sized LDs in comparison to the other tissues. Moreover, in the skeletal tissue, the ER displayed a specific form with a regular network structure surrounding numerous muscle fibers. In addition, the *in situ* fluorescence spectra of PPC or EPC in the LD and ER regions also showed results similar to those in live cells. Although LDs and the ER showed many differences in various tissues, there were still some common characteristics. (1) Despite their diverse sizes, the shape of LDs remained identical spherical. (2) LDs presented a close association to the ER, consistent with the observations from electron microscopy reported by many reports,[7,50] perhaps implying a certain interaction between them.

Visualization of the Interplay between LDs and the ER. To date, the mainstream hypothesis is that LDs originate from the ER; however, much more reliable proof to support this is still needed. In our work, by virtue of the water-sensitive probe PPC or EPC and the advanced Lambda scan mode, we successfully labeled different water-content LDs and the ER with orange and green fluorescence, respectively. Moreover, it has been reported that, during the formation of LDs, water is excluded to package the lipid efficiently to maintain the structural stability. According to the above facts, such a conjecture that the water content of nascent LDs is lower than that mature LDs should be reasonable. Thus, if the hypothesis that LDs are derived from the ER is valid, there should be two different color LDs in cells stained with PPC or EPC, due to their differences in water contents during the formation process. Typically, the nascent LDs should appear in the ER region and show green fluorescence similar to that in the ER, while mature LDs should display orange fluorescence. To testify to this, we carried out the following experiments.

First, the HeLa cells were pretreated with oleic acid to simulate LD formation[51] and then incubated with PPC or EPC. As shown in Figure 7, in addition to the orange LDs (indicated by the red arrows), several green dots (indicated by the blue arrows) occurred in the ER regions. These green dots showed a spherelike shape and a higher refractive index in DIC, the same characteristics as those of mature LDs, prehaps implying the nascent LDs. Moreover, the spectrum profile in green dots

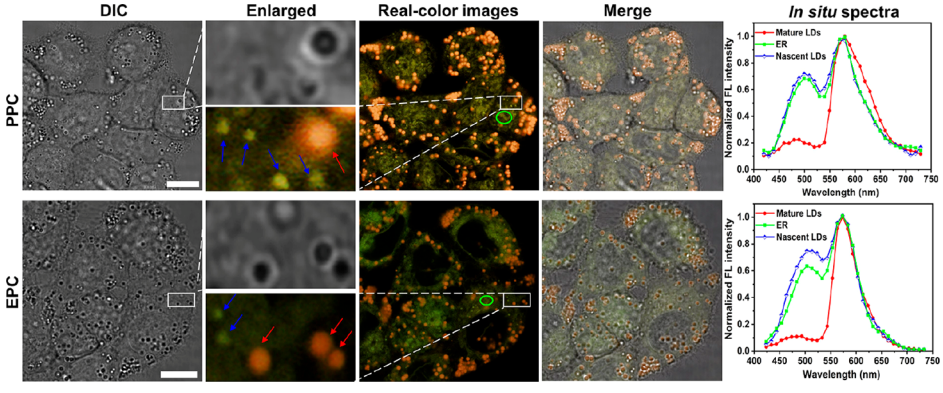

Figure 7. Real-color fluorescent images of oleic acid pretreated HeLa cells stained with PPC or EPC and the corresponding normalized *in situ* fluorescence spectra in nascent LDs (indicated by the blue arrows), mature LDs (indicated by the red arrows), and the ER (indicated by the green circles). λ_{ex} = 405 nm. Scale bar: 10 μm.

https://dx.doi.org/10.1021/jacs.0c12323
J. Am. Chem. Soc. 2021, 143, 3169−3179

closely resembled that in the ER (indicated by the green circles) but not the mature LDs (indicated by the red arrows).

To more intuitively illuminate the process of LD generation, we further performed Lambda mode based fluorescence imaging experiments by *in situ* and real-time two-color monitoring of the dynamics of LDs and ER in live cells. After treatment with oleic acid and incubation with PPC or EPC, the HeLa cells were directly imaged in the Lambda mode. As shown in Figure 8A and Video S1, the mature LDs and ER were clearly labeled by PPC with orange and green fluorescence, respectively. From the magnified images of the ROIs indicated by the white rectangles in Figure 8A (Figure 8B), we could see that there were no green dots in the ER region (indicated by the blue arrows) at the beginning. As time went on, a green-emissive dot began to be born near the ER region and gradually grew over 200 s. Moreover, the green dots showed the same *in situ* fluorescence spectra as those of ER (Figure 8C) but were obviously different from those of mature LDs. Likewise, cells stained with the probe EPC showed similar results, as shown in Figure S29 and Video S2.

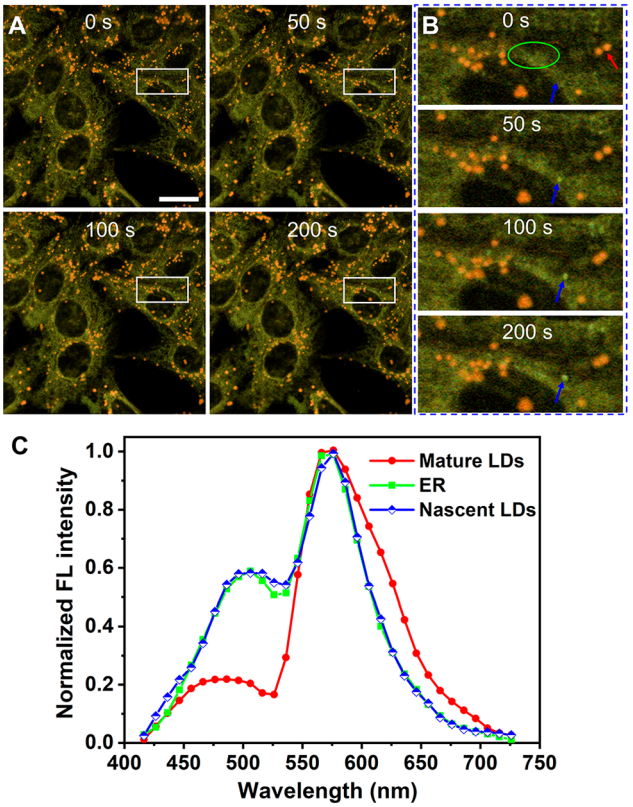

Figure 8. (A) *In situ* dynamic monitoring of LD formation in oleic acid pretreated HeLa cells stained with PPC at different time points. (B) Enlarged fluorescence images of the ROIs indicated by the white rectangles in (A). (C) *In situ* fluorescence spectra of mature LDs (indicated by the red arrow), ER (indicated by the green circles), and nascent LDs (indicated by the blue arrows). λ_{ex} = 405 nm. Scale bar: 20 μm.

To further verify that the newly born green dots were LDs, we conducted immunofluorescence imaging using anti-TIP47 antiserum labeled with Cy3-conjugated goat antirabbit IgG, because TIP47 is one of the specific sets of proteins existing on the phospholipid monolayer of both mature and nascent LDs in various cells.[52] As shown in Figure 9 and Figure S30, the imaging results showed that both orange and green dots stained with PPC or EPC were closely encircled by the red rings of the TIP47 protein. Meanwhile, the *in situ* fluorescence spectra also revealed that nascent LDs shared similar spectra to those in the ER, different from those in mature LDs. The similar fluorescence spectra indicate the similar water-containing environments between nascent LDs and the ER. Using PPC as an example, we also conducted colocalization experiments with anti-TIP47 and an ER-specific fluorescent immunostaining dye (Anti-Calreticulin antibody [EPR3924]-ER Marker (Alexa Fluor 647)). As shown in Figure S31, the ER regions stained with PPC showed a satisfying overlap with those stained with EPR3924. In addition, LDs with two different colors could merge with the dots labeled with anti-TIP47, which fully demonstrated the ability of simultaneous LD and ER staining of our probe. It should be noted that the dots labeled by TIP47 were also stained with EPR3924. This is most likely because EPR proteins not only mainly distribute on the ER but also exist on the phospholipid monolayer of LDs, given that the fact that a few proteins of the ER have been successively found on LDs.[7,53,54] When these results are taken together, the aforementioned *in situ* and real-time Lambda mode based fluorescence imaging and the immunofluorescence imaging data probably provide a very useful proof for the mainstream hypothesis that LDs originate from the ER.

CONCLUSION

In summary, we developed three ESIPT-active lipophilic fluorescent probes (PPC, EPC, and MNC) based on 3-hydroxyflavone via a facile synthesis. Due to their hydrophobic

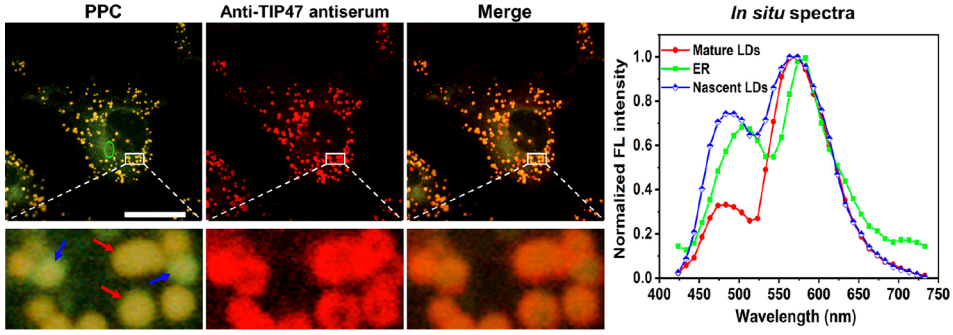

Figure 9. Real-color fluorescent images of oleic acid pretreated HeLa cells stained with PPC and anti-TIP47 antiserum and the corresponding normalized *in situ* fluorescence spectra in nascent LDs (indicated by the blue arrows), mature LDs (indicated by the red arrows), and ER (indicated by the green circle). PPC, λ_{ex} = 405 nm; anti-TIP47 antiserum (fluorescence from Cy3-conjugated goat antirabbit IgG), λ_{ex} = 561 nm. Scale bar: 20 μm.

https://dx.doi.org/10.1021/jacs.0c12323
J. Am. Chem. Soc. 2021, 143, 3169−3179

structure, they could simultaneously label incellular LDs and the ER. Among these probes, PPC snd EPC could achieve the two-color fluorescence imaging of LDs and ER in the Lambda mode, because of their supersensitive responses to slight water content changes, resulting in distinct color changes revealed by the CIE 1931 color coordinates. Such remarkable sensitivity benefits from their strong electron-donating substituents, which has been demonstrated by the ^{1}H NMR spectra and DFT calculations using MNC and PC as control probes. As a result, LDs and the ER in live cells and tissues have been clearly visualized by utilizing PPC or EPC, revealing their close apposition as well as specific morphology, volume, quantity, and distribution in different tissues. To the best of our knowledge, this is the first time that two-color fluorescence imaging of LDs and the ER in live samples using SF-probes has been realized. Further, the relationship between LD birth and the ER was investigated in live cells via the *in situ* and real-time imaging experiments, which reveal that the nascent LDs are generated near the ER regions and share an identical fluorescence color with that of the ER, probably providing a new and valuable proof for the hypothesis that LDs originate in the ER. We expect that our probes PPC and EPC can serve as novel and powerful imaging tools to uncover further interplays between LDs and the ER and decipher LD-ER related biological processes. Our work can also shed new light on the design strategy of future fluorescent probes for two-color imaging of other organelles and tracking of their interactions using advanced Lambda mode based fluorescnece imaging.

EXPERIMENTAL SECTION

General Information. Unless otherwise stated, all of the solvents and reagents were commercially available and were used without further purification. Silica column chromatography was conducted over silica gel using the SepaBean machine U200 from Santai Technologies Inc. MTT was purchased from Sigma. BODIPY 493/503, ER-Tracker Red, and SYTO 61 were purchased from Molecular Probes. The ^{1}H NMR and ^{13}C NMR spectra were recorded on a Bruker AVANCE III 400 MHz digital NMR spectrometer. The geometrically optimized structures of the molecules were calculated withthe Gaussian 09 package at B3LYP/6-31G level. The UV−visible−near-IR absorption spectra of dilute solutions were recorded on a Hitachi U-2910 spectrophotometer using a quartz cuvette of 1 cm path length. The fluorescence spectra were obtained on a Hitachi F-2700 spectrofluorimeter equipped with a 450 W Xe lamp. The spectral testing concentrations of PPC, EPC, and MNC were 2 μM. The CIE chromaticity coordinates were based on the spectral data. By calculation of the wavelength and corresponding intensity, the CIE chromaticity coordinates could be directly given by an FLS1000 photoluminescence spectrometer.

Cell Culture and Fluorescence Imaging. HeLa and SiHa cells were cultured in H-DMEM supplemented with 10% fetal bovine serum (FBS) and 1% penicillin and streptomycin. Mesenchymal stem cells (MSCs) were grown in alpha-MEM supplemented with 10% FBS and 1% penicillin and streptomycin. All of the above cells were cultured in a 5% CO_2 incubator at 37 °C. Before cell staining, all cells were plated on glass coverslips and allowed to adhere for 24 h.

For live cell staining experiments, the adherent cells were stained with PPC, EPC, or MNC (1 μM, 2 min) and then washed once with PBS and imaged. For costaining experiments, cells were stained with BODIPY 493/503 (5 μM, 30 min) or ER-Tracker Red (5 μM, 30 min) followed by rinsing twice with PBS; then the cells were further stained with PPC or EPC (1 μM, 2 min), washed once with PBS, and imaged.

Confocal fluorescence pseudocolor images and real-color images were obtained by a Nikon A1R confocal laser scanning microscope (CLSM) in the multichannel or Lambda mode. The Lambda scan mode is based on the spectral imaging function of confocal microscopy. This function enables the separate emission collection at different and limited wavelength ranges (for example, 10 nm) at each pixel. Each wavelength range is given an image with a certain intensity and proper pseudocolor as a function of fluorescence emission signal strength and wavelength. As a result, by plotting pixel intensity versus wavelength, the *in situ* fluorescence spectral profile of the dye can be readily acquired. When all images consisting of different collected wavelength bands were merged, a new image of nearly its real emission color (called the real-color image) could be obtained. The real-color images and *in situ* fluorescence spectra were acquired every 10 nm from 420 to 730 nm.

Cytotoxicity Measurements. The effects of PPC and EPC on cell viability were carried out using the standard MTT assay. SiHa cells growing in the log phase were seeded into 96-well plates (ca. 1×10^4 cells/well) and allowed to adhere for 24 h. Probes (100 μL/well) at different concentrations (1, 4, and 10 μM) for 24 h or at 1 μM for additional incubation times (2, 12, and 24 h) were placed in the wells of the treatment groups, and 100 μL/well DMSO diluted in DMEM at corresponding concentrations was added to the negative control group, respectively. Then 10 μL of MTT was placed in each well. After incubation for 4 h, the culture medium in each well was removed, and DMSO (100 μL) was added to dissolve the purple crystals. After 20 min, the absorbance was measured at 570 nm with a microplate reader. Finally, the cell survival rate could be calculated using the following equation: survival rate = $(A_{sample} - A_{blank})/(A_{DMSO} - A_{blank})$.

Tissue Staining. The various tissue blocks were directly removed from just killed adult Wistar rats and placed at room temperature in H-DMEM supplemented with 10% FBS and 1% penicillin and streptomycin. Then, the tissue blocks were stained with SYTO 61 (10 μM, 30 min) and PPC or EPC (5 μM, 10 min) and imaged with a Nikon A1R CLSM instrument. All of the above experiments were performed according to the international, national, and institutional rules concerning animal experiments, clinical studies, and biodiversity rights.

Dynamic Monitoring of LD Formation. First, HeLa cells were treated with 20 μM oleic acid and stained with 2 μM PPC or EPC without washing. Then the cells were observed using confocal microscopy in the Lambda mode. A real-color fluorescent image was obtained every 10 s during a time course of 200 s.

Immunofluorescence Method. HeLa cells were cultured on glass coverslips for 24 h and then pretreated with 40 μM oleic acid for 2 h. Next, the cells were fixed with 4% formaldehyde for 30 min, permeabilized with saponin, and blocked with 10% goat serum. After this, primary (antihuman TIP47 rabbit polyclonal antiserum, abbreviated as anti-TIP47 antiserum) and secondary (Alexa Fluor 594-conjugated goat antirabbit IgG) antibodies were placed sequentially in the cells. Finally, the cells were stained with 1 μM PPC or EPC for 2 min and imaged with a Nikon A1R CLSM instrument.

Synthetic Details. A mixture of compound **2** (0.5 mL, 4.1 mmol) and the equivalent compound **1** (**1a**−**d**) was added to a solution of EtOH (15 mL) in a flask. Next, 8 equiv of NaOH dissolved in 2 mL of water was placed in the flask. After the mixture was stirred for 24 h at room temperature, compound **3** (**3a**−**d**) was formed. Then 2 equiv of NaOH dissolved in 2 mL of water and 3 mL of 30% H_2O_2 were further added to this mixture. This mixture was stirred for 15 min at room temperature and then heated to 50 °C for 5 h. After it was cooled to room temperature, the reaction system was neutralized to neutral pH and then extracted with CH_2Cl_2 and washed with water three times. A yellow powder product was obtained after purification by silica gel chromatography and recrystallization with absolute EtOH.

Data for PPC (1.33 g, 80%) are as follows. ^{1}H NMR (400 MHz, DMSO-d_6): δ (ppm) 9.47 (s, 1H), 8.23−8.00 (m, 3H), 7.84−7.75 (m, 1H), 7.71 (d, J = 8.4 Hz, 1H), 7.46 (t, J = 7.5 Hz, 1H), 7.38 (t, J = 7.7 Hz, 4H), 7.19−7.09 (m, 6H), 7.05 (d, J = 8.7 Hz, 2H). ^{13}C NMR (100 MHz, DMSO-d_6): δ (ppm) 172.97, 154.90, 149.12, 146.86, 146.05, 138.75, 133.94, 130.26, 129.47, 125.95, 125.58, 125.20, 124.93, 124.68, 124.43, 121.87, 121.18, 118.71. HR-MS: calculated for $C_{27}H_{20}NO_3^+$ m/z 406.1438 ($[M + H]^+$), found 406.1451.

Data for EPC (0.99 g, 78%) are as follows. ^{1}H NMR (400 MHz, DMSO-d_6): δ (ppm) 9.15 (s, 1H), 8.10 (t, J = 8.3 Hz, 3H), 7.80−7.68

https://dx.doi.org/10.1021/jacs.0c12323
J. Am. Chem. Soc. 2021, 143, 3169−3179

(m, 2H), 7.48−7.40 (m, 1H), 6.81 (d, J = 9.1 Hz, 2H), 3.43 (q, J = 7.0 Hz, 4H), 1.14 (t, J = 7.0 Hz, 6H). ^{13}C NMR (100 MHz, DMSO-d_6): δ (ppm) 172.29, 154.70, 148.92, 147.46, 137.56, 133.46, 131.39, 129.76, 128.26, 125.08, 124.73, 121.94, 118.55, 117.47, 111.25, 44.17, 12.93. HR-MS: calculated for $C_{19}H_{20}NO_3^+$ m/z 310.1438 ([M + H]$^+$), found 310.1492.

Data for MNC (0.98 g, 75%) are as follows. ^{1}H NMR (400 MHz, DMSO-d_6): δ (ppm) 9.69 (s, 1H), 8.76 (s, 1H), 8.31 (d, J = 8.6 Hz, 1H), 8.15 (d, J = 7.9 Hz, 1H), 7.99 (d, J = 8.7 Hz, 2H), 7.83 (d, J = 3.9 Hz, 2H), 7.54−7.45 (m, 1H), 7.42 (d, J = 1.2 Hz, 1H), 7.25 (dd, J = 8.9, 2.0 Hz, 1H), 3.93 (s, 3H). ^{13}C NMR (100 MHz, DMSO-d_6): δ (ppm) 173.30, 159.08, 155.11, 146.06, 139.49, 135.25, 134.13, 130.97, 128.34, 128.28, 127.31, 126.92, 125.36, 125.28, 125.03, 121.86, 119.88, 118.89, 106.42, 55.83. HR-MS: calculated for $C_{20}H_{15}O_4^+$ m/z 319.0965 ([M + H]$^+$), found 319.0950.

Data for PC (1.11 g, 80%) are as follows. ^{1}H NMR (400 MHz, DMSO-d_6): δ (ppm) 9.64 (s, 1H), 8.30−8.19 (m, 2H), 8.13 (dd, J = 8.0, 1.0 Hz, 1H), 7.87−7.73 (m, 2H), 7.63−7.55 (m, 2H), 7.55−7.44 (m, 2H). ^{13}C NMR (100 MHz, $CDCl_3$): δ (ppm) 172.47, 154.40, 143.89, 137.44, 132.63, 130.04, 129.17, 127.58, 126.73, 124.44, 123.50, 119.60, 117.27. HR-MS: calculated for $C_{15}H_9O_3^-$ m/z 237.0557 ([M − H]$^-$), found 237.0544.

■ ASSOCIATED CONTENT

Supporting Information

The Supporting Information is available free of charge at https://pubs.acs.org/doi/10.1021/jacs.0c12323.

In situ and real-time Lambda mode based fluorescence imaging of PPC in oleic acid pretreated HeLa cells (AVI)
In situ and real-time Lambda mode based fluorescence imaging of EPC in oleic acid pretreated HeLa cells (AVI)
Synthesis routes, ^{1}H NMR, ^{13}C NMR, and HRMS spectra, photophysical data, and imaging data (PDF)

■ AUTHOR INFORMATION

Corresponding Authors

Guangle Niu − *State Key Laboratory of Crystal Materials, and Advanced Medical Research Institute, Shandong University, Jinan 250100, People's Republic of China; Shenzhen Research Institute of Shandong University, Shenzhen 518057, People's Republic of China;* orcid.org/0000-0002-5403-6880; Email: niugl@sdu.edu.cn

Xiaoqiang Yu − *State Key Laboratory of Crystal Materials, and Advanced Medical Research Institute, Shandong University, Jinan 250100, People's Republic of China; Shenzhen Research Institute of Shandong University, Shenzhen 518057, People's Republic of China;* orcid.org/0000-0002-4313-6464; Email: yuxq@sdu.edu.cn

Authors

Lifang Guo − *State Key Laboratory of Crystal Materials, and Advanced Medical Research Institute, Shandong University, Jinan 250100, People's Republic of China; Key Laboratory for Advanced Materials and Joint International Research Laboratory of Precision Chemistry and Molecular Engineering, Feringa Nobel Prize Scientist Joint Research Center, East China University of Science & Technology, Shanghai 200237, People's Republic of China; Shenzhen Research Institute of Shandong University, Shenzhen 518057, People's Republic of China*

Minggang Tian − *State Key Laboratory of Crystal Materials, and Advanced Medical Research Institute, Shandong University, Jinan 250100, People's Republic of China*

Zhiyun Zhang − *Key Laboratory for Advanced Materials and Joint International Research Laboratory of Precision Chemistry and Molecular Engineering, Feringa Nobel Prize Scientist Joint Research Center, East China University of Science & Technology, Shanghai 200237, People's Republic of China;* orcid.org/0000-0001-7513-9427

Qing Lu − *State Key Laboratory of Crystal Materials, and Advanced Medical Research Institute, Shandong University, Jinan 250100, People's Republic of China*

Zhiqiang Liu − *State Key Laboratory of Crystal Materials, and Advanced Medical Research Institute, Shandong University, Jinan 250100, People's Republic of China;* orcid.org/0000-0001-7863-1759

Complete contact information is available at: https://pubs.acs.org/10.1021/jacs.0c12323

Author Contributions

All authors have reviewed and approved the final version of this manuscript.

Notes

The authors declare no competing financial interest.

■ ACKNOWLEDGMENTS

Our laser confocal scanning imaging of living cells was performed at The Microscopy Characterization Facility, Shandong University. The study was financially supported by the National Natural Science Foundation of China (52073163, 51773111, 21672130, 51273107 and 22004036), the Natural Science Foundation of Shandong Province, China (ZR2017ZC0227), the Fundamental Research Funds of Shandong University (2017JC011 and 2018JC030), the Special Fund of Taishan Scholars Project of Shandong Province, China (tsqn201909012), the Guangdong Basic and Applied Basic Research Foundation (2020A1515110578), the Opening Fund of Key Laboratory of Photochemical Conversion and Optoelectronic Materials, TIPC, CAS (PCOM202001), and the Program of Qilu Young Scholars of Shandong University. We also sincerely thank Prof. Dongfeng Xue at Shandong University for providing valuable advices and discussions to further improve the quality of this work.

■ REFERENCES

(1) Xu, W.; Zeng, Z.; Jiang, J.-H.; Chang, Y.-T.; Yuan, L. Discerning the chemistry in individual organelles with small-molecule fluorescent probes. *Angew. Chem., Int. Ed.* **2016**, *55*, 13658; *Angew. Chem.* **2016**, *128*, 13858.
(2) Zhu, H.; Fan, J.; Du, J.; Peng, X. Fluorescent probes for sensing and imaging within specific cellular organelles. *Acc. Chem. Res.* **2016**, *49*, 2115.
(3) Wang, L.; Frei, M. S.; Salim, A.; Johnsson, K. Small-molecule fluorescent probes for live-cell super-resolution microscopy. *J. Am. Chem. Soc.* **2019**, *141*, 2770.
(4) Alberts, B.; Johnson, A.; Lewis, J.; Raff, M.; Roberts, K.; Walter, P. *Molecular Biology of the Cell*, 5th ed.; Garland Science: New York, 2008; Vol. *40*, p 1709.
(5) Tagaya, M.; Simmen, T. *Organelle contact sites*; Springer Singapore: 2017; Vol. *997*, p p 111.
(6) Gao, Q.; Goodman, J. M. The lipid droplet-a well-connected organelle. *Front. Cell Dev. Biol.* **2015**, *3*, 49.
(7) Farese, R. V., Jr.; Walther, T. C. Lipid droplets finally get a little R-E-S-P-E-C-T. *Cell* **2009**, *139*, 855.
(8) Beller, M.; Thiel, K.; Thul, P. J.; Jäckle, H. Lipid droplets: A dynamic organelle moves into focus. *FEBS Lett.* **2010**, *584*, 2176.
(9) Thiele, C.; Spandl, J. Cell biology of lipid droplets. *Curr. Opin. Cell Biol.* **2008**, *20*, 378.

(10) Zhang, J.; Wang, J.; Tian, H. Taking orders from light: progress in photochromic bio-materials. *Mater. Horiz.* **2014**, *1*, 169.
(11) Zheng, X.; Ge, J.; Wu, J.; Liu, W.; Guo, L.; Jia, Q.; Ding, Y.; Zhang, H.; Wang, P. Biodegradable hypocrellin derivative nanovesicle as a near-infrared light-driven theranostic for dually photoactive cancer imaging and therapy. *Biomaterials* **2018**, *185*, 133.
(12) Chen, M.; Hu, X.; Liu, J.; Li, B.; Leung, N. L. C.; Viglianti, L.; Cheung, T. S.; Sung, H. H. Y.; Kwok, R. T. K.; Williams, I. D.; Qin, A.; Lam, J. W. Y.; Tang, B. Z. Rational design of red AIEgens with a new core structure from non-emissive heteroaromatics. *Chem. Sci.* **2018**, *9*, 7829.
(13) Fu, W.; Yan, C.; Guo, Z.; Zhang, J.; Zhang, H.; Tian, H.; Zhu, W.-H. Rational design of near-infrared aggregation-induced-emission-active probes: in situ mapping of amyloid-β plaques with ultrasensitivity and high-fidelity. *J. Am. Chem. Soc.* **2019**, *141*, 3171.
(14) Xia, F.; Wu, J.; Wu, X.; Hu, Q.; Dai, J.; Lou, X. Modular design of peptide- or DNA-modified AIEgen probes for biosensing applications. *Acc. Chem. Res.* **2019**, *52*, 3064.
(15) Xiao, H.; Zhang, W.; Li, P.; Zhang, W.; Wang, X.; Tang, B. Versatile fluorescent probes for imaging the superoxide anion in living cells and in vivo. *Angew. Chem., Int. Ed.* **2020**, *59*, 4216; *Angew. Chem.* **2020**, *132*, 4244.
(16) Fang, H.; Yao, S.; Chen, Q.; Liu, C.; Cai, Y.; Geng, S.; Bai, Y.; Tian, Z.; Zacharias, A. L.; Takebe, T.; Chen, Y.; Guo, Z.; He, W.; Diao, J. De novo-designed near-infrared nanoaggregates for super-resolution monitoring of lysosomes in cells, in whole organoids, and in vivo. *ACS Nano* **2019**, *13*, 14426.
(17) Zang, T.; Xie, Y.; Su, S.; Liu, F.; Chen, Q.; Jing, J.; Zhang, R.; Niu, G.; Zhang, X. In vitro light-up visualization of a subunit-specific enzyme by an AIE probe via restriction of single molecular motion. *Angew. Chem., Int. Ed.* **2020**, *59*, 10003; *Angew. Chem.* **2020**, *132*, 10089.
(18) Dang, D.; Liu, H.; Wang, J.; Chen, M.; Liu, Y.; Sung, H. H. Y.; Williams, I. D.; Kwok, R. T. K.; Lam, J. W. Y.; Tang, B. Z. Highly emissive AIEgens with multiple functions: facile synthesis, chromism, specific lipid droplet imaging, apoptosis monitoring, and in vivo imaging. *Chem. Mater.* **2018**, *30*, 7892.
(19) Shi, L.; Li, K.; Li, L.-L.; Chen, S.-Y.; Li, M.-Y.; Zhou, Q.; Wang, N.; Yu, X.-Q. Novel easily available purine-based AIEgens with colour tunability and applications in lipid droplet imaging. *Chem. Sci.* **2018**, *9*, 8969.
(20) Collot, M.; Fam, T. K.; Ashokkumar, P.; Faklaris, O.; Galli, T.; Danglot, L.; Klymchenko, A. S. Ultrabright and fluorogenic probes for multicolor imaging and tracking of lipid droplets in cells and tissues. *J. Am. Chem. Soc.* **2018**, *140*, 5401.
(21) Fam, T. K.; Klymchenko, A. S.; Collot, M. Recent advances in fluorescent probes for lipid droplets. *Materials* **2018**, *11*, 1768.
(22) Zhao, N.; Li, Y.; Yang, W.; Zhuang, J.; Li, Y.; Li, N. Multifunctional pyrazoline based AIEgens: real-time tracking and specific protein "fishing" of lipid droplets. *Chem. Sci.* **2019**, *10*, 9009.
(23) Zheng, X.; Zhu, W.; Ni, F.; Ai, H.; Gong, S.; Zhou, X.; Sessler, J. L.; Yang, C. Simultaneous dual-colour tracking lipid droplets and lysosomes dynamics using a fluorescent probe. *Chem. Sci.* **2019**, *10*, 2342.
(24) Cho, M. K.; Seo, M. J.; Juvekar, V.; Jo, J. H.; Kim, W.; Choi, K. S.; Kim, H. M. Screening of drug-induced steatosis and phospholipidosis using lipid droplet-selective two-photon probes. *Anal. Chem.* **2020**, *92*, 11223.
(25) Jiang, G.; Jin, Y.; Li, M.; Wang, H.; Xiong, M.; Zeng, W.; Yuan, H.; Liu, C.; Ren, Z.; Liu, C. Faster and more specific: excited-state intramolecular proton transfer-based dyes for high-fidelity dynamic imaging of lipid droplets within cells and tissues. *Anal. Chem.* **2020**, *92*, 10342.
(26) Zhang, C.-J.; Cai, X.; Xu, S.; Zhan, R.; Jien, W.; Liu, B. A light-up endoplasmic reticulum probe based on a rational design of red-emissive fluorogens with aggregation-induced emission. *Chem. Commun.* **2017**, *53*, 10792.
(27) Benhamou, R. I.; Jaber, Q. Z.; Herzog, I. M.; Roichman, Y.; Fridman, M. Fluorescent tracking of the endoplasmic reticulum in live pathogenic fungal cells. *ACS Chem. Biol.* **2018**, *13*, 3325.
(28) Huang, C.; Li, T.; Liang, J.; Huang, H.; Zhang, P.; Banerjee, S. Recent advances in endoplasmic reticulum targeting metal complexes. *Coord. Chem. Rev.* **2020**, *408*, 213178.
(29) Alam, P.; He, W.; Leung, N. L. C.; Ma, C.; Kwok, R. T. K.; Lam, J. W. Y.; Sung, H. H. Y.; Williams, I. D.; Wong, K. S.; Tang, B. Z. Red AIE-active fluorescent probes with tunable organelle-specific targeting. *Adv. Funct. Mater.* **2020**, *30*, 1909268.
(30) Nagy, L. I.; Molnár, E.; Kanizsai, I.; Madácsi, R.; Ózsvári, B.; Fehér, L. Z.; Fábián, G.; Marton, A.; Vizler, C.; Ayaydin, F.; Kitajka, K.; Hackler, L.; Mátés, L.; Deák, F.; Kiss, I.; Puskás, L. G. Lipid droplet binding thalidomide analogs activate endoplasmic reticulum stress and suppress hepatocellular carcinoma in a chemically induced transgenic mouse model. *Lipids Health Dis.* **2013**, *12*, 175.
(31) Foissner, I. Fluorescent phosphocholine-a specific marker for the endoplasmic reticulum and for lipid droplets in Chara internodal cells. *Protoplasma* **2009**, *238*, 47.
(32) Brelje, T. C.; Wessendorf, M. W.; Sorenson, R. L. Multicolor laser scanning confocal immunofluorescence microscopy: practical application and limitations. *Methods Cell Biol.* **1993**, *38*, 97.
(33) Zhuo, S.; Chen, J.; Luo, T.; Zou, D.; Zhao, J. Multimode nonlinear optical imaging of the dermis in ex vivo human skin based on the combination of multichannel mode and Lambda mode. *Opt. Express* **2006**, *14*, 7810.
(34) Niu, G.; Zheng, X.; Zhao, Z.; Zhang, H.; Wang, J.; He, X.; Chen, Y.; Shi, X.; Ma, C.; Kwok, R. T. K.; Lam, J. W. Y.; Sung, H. H. Y.; Williams, I. D.; Wong, K. S.; Wang, P.; Tang, B. Z. Functionalized acrylonitriles with aggregation-induced emission: structure tuning by simple reaction-condition variation, efficient red emission, and two-photon bioimaging. *J. Am. Chem. Soc.* **2019**, *141*, 15111.
(35) Jiang, X.; Zhong, J.; Liu, Y.; Yu, H.; Zhuo, S.; Chen, J. Two-photon fluorescence and second-harmonic generation imaging of collagen in human tissue based on multiphoton microscopy. *Scanning* **2011**, *33*, 53.
(36) Thiam, A. R.; Farese, R. V., Jr.; Walther, T. C. The biophysics and cell biology of lipid droplets. *Nat. Rev. Mol. Cell Biol.* **2013**, *14*, 775.
(37) Sedgwick, A. C.; Wu, L.; Han, H.-H.; Bull, S. D.; He, X.-P.; James, T. D.; Sessler, J. L.; Tang, B. Z.; Tian, H.; Yoon, J. Excited-state intramolecular proton-transfer (ESIPT) based fluorescence sensors and imaging agents. *Chem. Soc. Rev.* **2018**, *47*, 8842.
(38) Demchenko, A. P.; Tang, K.-C.; Chou, P.-T. Excited-state proton coupled charge transfer modulated by molecular structure and media polarization. *Chem. Soc. Rev.* **2013**, *42*, 1379.
(39) Wu, J.; Liu, W.; Ge, J.; Zhang, H.; Wang, P. New sensing mechanisms for design of fluorescent chemosensors emerging in recent years. *Chem. Soc. Rev.* **2011**, *40*, 3483.
(40) Demchenko, A. P.; Mely, Y.; Duportail, G.; Klymchenko, A. S. Monitoring biophysical properties of lipid membranes by environment-sensitive fluorescent probes. *Biophys. J.* **2009**, *96*, 3461.
(41) Klymchenko, A. S.; Pivovarenko, V. G.; Ozturk, T.; Demchenko, A. P. Modulation of the solvent-dependent dual emission in 3-hydroxychromones by substituents. *New J. Chem.* **2003**, *27*, 1336.
(42) Klymchenko, A. S.; Demchenko, A. P. Multiparametric probing of intermolecular interactions with fluorescent dye exhibiting excited state intramolecular proton transfer. *Phys. Chem. Chem. Phys.* **2003**, *5*, 461.
(43) Klymchenko, A. S.; Mely, Y. Fluorescent environment-sensitive dyes as reporters of biomolecular interactions. *Prog. Mol. Biol. Transl. Sci.* **2013**, *113*, 35.
(44) Shynkar, V. V.; Klymchenko, A. S.; Duportail, G.; Demchenko, A. P.; Mely, Y. Two-color fluorescent probes for imaging the dipole potential of cell plasma membranes. *Biochim. Biophys. Acta. Biochim. Biophys. Acta, Biomembr.* **2005**, *1712*, 128.
(45) Shynkar, V. V.; Klymchenko, A. S.; Kunzelmann, C.; Duportail, G.; Muller, C. D.; Demchenko, A. P.; Freyssinet, J. M.; Mely, Y. Fluorescent biomembrane probe for ratiometric detection of apoptosis. *J. Am. Chem. Soc.* **2007**, *129*, 2187.
(46) Ishikawa, M.; Hashimoto, Y. Improvement in aqueous solubility in small molecule drug discovery programs by disruption of molecular planarity and symmetry. *J. Med. Chem.* **2011**, *54*, 1539.

https://dx.doi.org/10.1021/jacs.0c12323
J. Am. Chem. Soc. 2021, 143, 3169−3179

(47) Frisch, M. J.; Trucks, G. W.; Schlegel, H. B.; Scuseria, G. E.; Robb, M. A.; Cheeseman, J.; Scalmani, G.; Barone, V.; Mennucci, B.; Petersson, G. A.; Nakatsuji, H.; Caricato, M.; Li, X.; Hratchian, H. P.; Izmaylov, A. F., et al. *Gaussian 09, rev. 1A*; Gaussian Inc.: Wallingford, CT, 2009.
(48) Smith, T.; Guild, J. The C.I.E. colorimetric standards and their use. *Trans. Opt. Soc.* **1932**, *33*, 73.
(49) Pampaloni, F.; Reynaud, E. G.; Stelzer, E. H. K. The third dimension bridges the gap between cell culture and live tissue. *Nat. Rev. Mol. Cell Biol.* **2007**, *8*, 839.
(50) Murphy, S.; Martin, S.; Parton, R. G. Lipid droplet-organelle interactions; sharing the fats. *Biochim. Biophys. Acta, Mol. Cell Biol. Lipids* **2009**, *1791*, 441.
(51) Grillitsch, K.; Connerth, M.; Kofeler, H.; Arrey, T. N.; Rietschel, B.; Wagner, B.; Karas, M.; Daum, G. Lipid particles/droplets of the yeast Saccharomyces cerevisiae revisited: lipidome meets proteome. *Biochim. Biophys. Acta, Mol. Cell Biol. Lipids* **2011**, *1811*, 1165.
(52) Murphy, D. J. The biogenesis and functions of lipid bodies in animals, plants and microorganisms. *Prog. Lipid Res.* **2001**, *40*, 325.
(53) Cermelli, S.; Guo, Y.; Gross, S. P.; Welte, M. A. The Lipid-Droplet Proteome Reveals that Droplets Are a Protein-Storage Depot. *Curr. Biol.* **2006**, *16*, 1783.
(54) Ozeki, S.; Cheng, J.; Tauchi-Sato, K.; Hatano, N.; Taniguchi, H.; Fujimoto, T. Rab18 localizes to lipid droplets and induces their close apposition to the endoplasmic reticulum-derived membrane. *J. Cell Sci.* **2005**, *118*, 2601.

https://dx.doi.org/10.1021/jacs.0c12323
J. Am. Chem. Soc. 2021, 143, 3169−3179